

Spatial instability of flow in a semiinfinite cylinder with fluid injection through its porous walls

Jérôme Griffond, Grégoire Casalis *, Jean-Philippe Pineau

ONERA-CERT, Aerodynamics and Energetics Modeling Department, 2 avenue Ed. Belin, B.P. 4025, 31055 Toulouse cedex 4, France

(Received 15 January 1999; revised 12 April 1999; accepted 10 May 1999)

Abstract – In this article, the stability of incompressible pipe flows induced by wall injection is investigated. A local linear spatial theory is applied with a special treatment near the axis due to the choice of the cylindrical coordinates. It shows that the flow is stable near the headwall until it reaches a critical axial position. The flow becomes unstable downstream for a range of frequencies which increases with the distance to the headwall. Unstable two-dimensional and also three-dimensional modes are exhibited. Comparison with the available experimental results confirms the existence of amplified instability waves and the presence of at least some of the predicted modes. © 2000 Éditions scientifiques et médicales Elsevier SAS

linear stability / injection induced flows / pipe flows

1. Introduction

Several solid-propellant motors exhibit oscillatory behaviours of longitudinal acoustic modes although they are predicted to be stable by means of conventional methods, such as the acoustic balance. New sources of acoustic energy have to be found to explain this phenomenon. Since the conditions of pressure and temperature inside the combustion chamber allow only very few measurements, specific experiments have been designed for simulating the behaviour of solid-propellant motors. They use cold gas injected through porous walls with various channel geometries, see for example Brown et al. [1] and Avalon et al. [2]. Therefore, neither high temperature or diphasic effects nor chemical reactions can occur. The generated simplified flow has been also numerically studied, see Lupoglazoff et al. [3] and an intrinsic instability mechanism of flows induced by injection through porous-walled ducts has been discovered which is regarded as a possible cause for the oscillatory behaviour of the motor.

The pioneer work on this subject is due to Varapaev et al. [4] who treated the case of a two-dimensional planar geometry. Then numerical investigations led by Lupoglazoff et al. [5] illuminated the aero-acoustic phenomenon involving the instability mechanism.

In a previous article [6], a two-dimensional linear stability theory has been applied to planar ducts and the results were successfully compared with measurements performed in a cold-gas experiment with a parallelepipedic channel. The laminar, incompressible and inviscid mean flow is stable up to a critical abscissa and becomes unstable downstream. Then due to the good agreement between the experiment and the theoretical stability predictions and the occurrence of acoustic resonance under some conditions, a scenario and a criterion have been suggested for the coupling between the intrinsic instability and longitudinal acoustic modes, see [7].

* Correspondence and reprints; email: casalis@oncert.fr

The purpose of the present paper is to extend this linear stability theory to cylindrical ducts. We first present the equations, the geometry and the mean flow (or basic flow) of the axisymmetric problem. Then, we pursue the stability analysis based on the small perturbations decomposition with a normal mode form for the perturbation. In the next section, we present the numerical resolution method and the treatment of the singularity on the axis. Section 5 is devoted to the presentation of the numerical results. We mainly present the neutral curves for two- and three-dimensional modes. As in the planar case, this leads to a critical frequency associated to a critical distance from the headwall, downstream of which the basic flow is unstable. Finally, we compare our results with the experimental ones published by Dunlap et al. [8]. Spectra, fluctuation profiles and spatial amplification are compared to the available results but unfortunately the latter were not designed to explicitly check out stability mechanism so that no quantitative nor definitive proof of the validity of the theory can be given.

2. Presentation of the flow and notations

2.1. Geometry and coordinate system

The considered flow is induced by wall injection in a cylindrical channel of radius a , represented in *figure 1*. The channel is limited upstream by a nonporous front wall called the headwall. At the porous walls, the injection velocity, denoted by V_{inj} , is supposed to be perpendicular to the wall, uniform and constant. We use the cylindrical system of coordinates (x, r, θ) with x along the axis of the channel, directed from the headwall to the exhaust. The origin is chosen at the headwall ($x = 0$). The corresponding components of the velocity vector are denoted by (U_x, U_r, U_θ) .

2.2. Governing equations

The study is restricted to incompressible, monophasic and nonreactive flows and the gravity is neglected. The governing equations are the following nondimensionalised Navier–Stokes equations:

$$\left\{ \begin{array}{l} \frac{\partial U_x}{\partial x} + \frac{\partial U_r}{\partial r} + \frac{U_r}{r} + \frac{1}{r} \frac{\partial U_\theta}{\partial \theta} = 0, \\ \frac{\partial U_x}{\partial t} + U_x \frac{\partial U_x}{\partial x} + U_r \frac{\partial U_x}{\partial r} + \frac{U_\theta}{r} \frac{\partial U_x}{\partial \theta} + \frac{\partial P}{\partial x} = \frac{1}{\mathcal{R}_{inj}} \left(\frac{\partial^2 U_x}{\partial x^2} + \frac{\partial^2 U_x}{\partial r^2} + \frac{1}{r} \frac{\partial U_x}{\partial r} + \frac{1}{r^2} \frac{\partial^2 U_x}{\partial \theta^2} \right), \\ \frac{\partial U_r}{\partial t} + U_x \frac{\partial U_r}{\partial x} + U_r \frac{\partial U_r}{\partial r} + \frac{U_\theta}{r} \frac{\partial U_r}{\partial \theta} - \frac{U_\theta^2}{r} + \frac{\partial P}{\partial r} \\ = \frac{1}{\mathcal{R}_{inj}} \left(\frac{\partial^2 U_r}{\partial x^2} + \frac{\partial^2 U_r}{\partial r^2} + \frac{1}{r} \frac{\partial U_r}{\partial r} - \frac{U_r}{r^2} + \frac{1}{r^2} \frac{\partial^2 U_r}{\partial \theta^2} - \frac{2}{r^2} \frac{\partial U_\theta}{\partial \theta} \right), \\ \frac{\partial U_\theta}{\partial t} + U_x \frac{\partial U_\theta}{\partial x} + U_r \frac{\partial U_\theta}{\partial r} + \frac{U_\theta}{r} \frac{\partial U_\theta}{\partial \theta} + \frac{U_r U_\theta}{r} + \frac{1}{r} \frac{\partial P}{\partial \theta} \\ = \frac{1}{\mathcal{R}_{inj}} \left(\frac{\partial^2 U_\theta}{\partial x^2} + \frac{\partial^2 U_\theta}{\partial r^2} + \frac{1}{r} \frac{\partial U_\theta}{\partial r} - \frac{U_\theta}{r^2} + \frac{1}{r^2} \frac{\partial^2 U_\theta}{\partial \theta^2} + \frac{2}{r^2} \frac{\partial U_r}{\partial \theta} \right), \end{array} \right. \quad (1)$$

where \mathcal{R}_{inj} represents the Reynolds number:

$$\mathcal{R}_{inj} = \frac{V_{inj} a}{\nu}$$

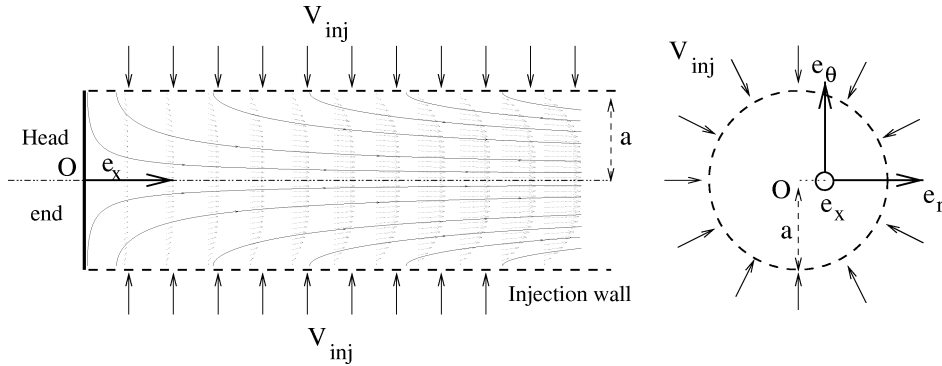


Figure 1. Streamlines, velocity vectors of the flow and main notations.

with ν being the kinematic velocity. These equations have been made dimensionless by using the reference length a (the radius) and the reference velocity V_{inj} . In the following all the distances are made dimensionless by using the radius a , whereas the reference length in [8] is the diameter $D = 2a$.

The associated nondimensionalised boundary conditions are:

$$\forall r, \forall \theta, \forall t \quad \begin{cases} U_x(x = 0, r, \theta, t) = 0, \\ U_r(x = 0, r, \theta, t) = 0, \\ U_\theta(x = 0, r, \theta, t) = 0, \end{cases} \quad \forall x, \forall \theta, \forall t \quad \begin{cases} U_x(x, r = 1, \theta, t) = 0, \\ U_r(x, r = 1, \theta, t) = -1, \\ U_\theta(x, r = 1, \theta, t) = 0. \end{cases}$$

2.3. Mean flow

An exact solution can be searched by looking for a nondimensionalised Stokes stream function of self-similar form

$$\Psi = \frac{x F(r)}{\mathcal{R}_{inj}}, \quad \bar{U}_x = \frac{x F'(r)}{r \mathcal{R}_{inj}}, \quad \bar{U}_r = -\frac{1}{r} \frac{F(r)}{\mathcal{R}_{inj}}, \quad (2)$$

which gives the fourth order differential equation:

$$\left(\frac{F'}{r}\right)''' + \left[\left(\frac{1}{r} + \frac{F}{r}\right)\left(\frac{F'}{r}\right)' - \left(\frac{F'}{r}\right)\left(\frac{F'}{r}\right)'\right] = 0$$

with the boundary conditions:

$$\begin{cases} \frac{F'}{r} = 0, & \frac{F}{r} = \mathcal{R}_{inj} & \text{for } r = 1, \\ \left(\frac{F'}{r}\right)' = 0, & \frac{F}{r} = 0 & \text{for } r = 0. \end{cases}$$

These equations can be numerically solved and they provide the solution of the complete Navier–Stokes equations. However, Taylor obtained an analytical solution of the inviscid Euler equations, see [9]:

$$\begin{cases} \bar{U}_x = \pi x \cos\left(\frac{\pi}{2}r^2\right), \\ \bar{U}_r = -\frac{1}{r} \sin\left(\frac{\pi}{2}r^2\right), \\ \bar{U}_\theta = 0, \end{cases} \quad (3)$$

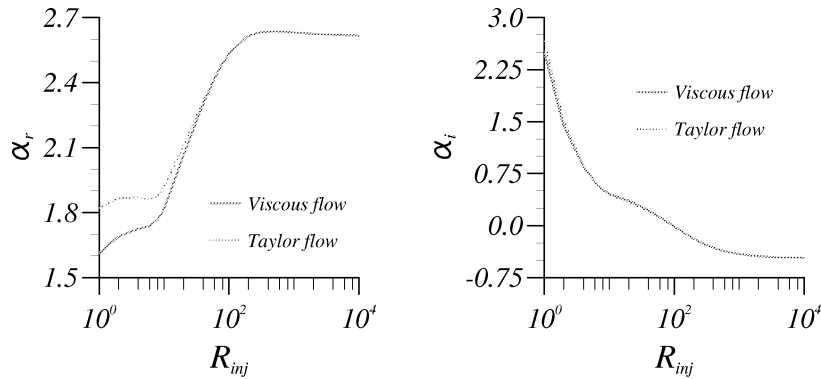


Figure 2. Effect of the inviscid Taylor flow approximation on stability results: wavenumber (left part), amplification rate (right part), versus the injection Reynolds number. $x = 10$, $\omega = 50$, $q = 0$.

which is a good approximation of the viscous flow for the Reynolds numbers of interest ($\mathcal{R}_{inj} > 1000$) and will be referred to as ‘Taylor flow’. *Figure 2* shows that the Taylor flow (3) provides stability results, see next section, which cannot be distinguished from the viscous flow (2) as soon as the Reynolds number becomes greater than one hundred, typically.

3. Linear stability theory

3.1. Perturbation form

The first step of the stability study requires the small perturbation technique: each quantity is written as a superposition of a mean quantity (here, the quantity obtained from the known steady Taylor flow) and of a fluctuating quantity:

$$(U_x, U_r, U_\theta, P)(x, r, \theta, t) = (\overline{U}_x, \overline{U}_r, \overline{U}_\theta, \overline{P})(x, r) + (u_x, u_r, u_\theta, p)(x, r, \theta, t). \quad (4)$$

The fluctuating quantities are assumed to be small relative to the mean ones. The Navier–Stokes equations and the boundary conditions are rewritten using this decomposition. They are then simplified by taking into account that the mean flow satisfies them. They are finally linearised by dropping the nonlinear fluctuating terms.

The linearized boundary conditions are homogeneous, namely:

$$u_x(1) = u_r(1) = u_\theta(1) = 0.$$

The problem is further simplified by choosing an adequate form for the disturbances. The independence of the mean flow and of the boundary conditions with respect to the time and to the azimuthal coordinate suggests an exponential dependence with respect to these coordinates (normal mode).

Concerning the streamwise coordinate, the mean flow is proportional to it so that the normal mode form $e^{i\alpha x}$ used to obtain the Orr–Sommerfeld equation is not valid a priori. As for the two-dimensional case in [6], three approaches can be developed: a local strictly parallel theory (OSE: Orr–Sommerfeld Equations), a local nonconsistent approach in which the terms \overline{U}_r and $\partial \overline{U}_x / \partial x$ are kept (LNP: Local NonParallel) and consistent nonlocal calculations using the ‘Parabolized Stability Equations’ (PSE) with a normalization based on the

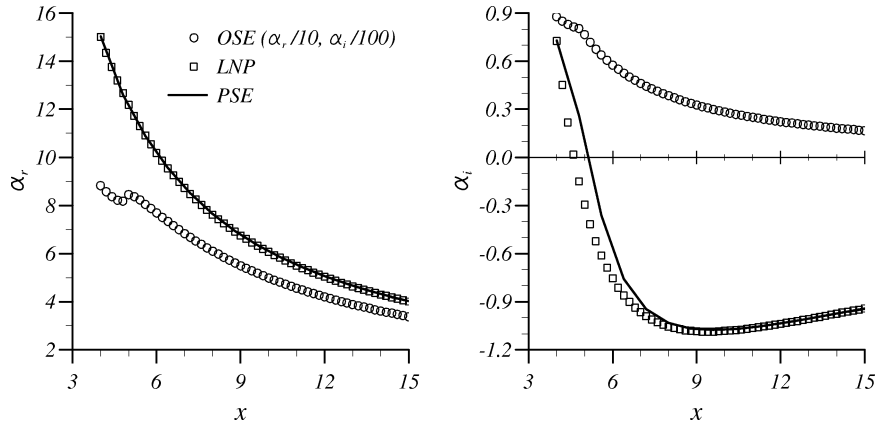


Figure 3. Comparison of the wavenumber and the growth rate, versus the abscissa, obtained by the Orr–Sommerfeld equation (OSE), the local nonparallel approach (LNP) and the nonlocal parabolized stability equations (PSE). $\omega = 80$, $q = 0$, $\mathcal{R}_{inj} = 4500$.

energy of the perturbation, see Herbert et al. [10]. The two first approaches use the normal mode for the perturbation:

$$(u_x, u_r, u_\theta, p)(x, r, \theta, t) = (\hat{u}_x, \hat{u}_r, \hat{u}_\theta, \hat{p})(r)e^{i(\alpha x + q\theta - \omega t)}, \quad (5)$$

whereas the third one uses a generalized form of (5), see [10].

A spatial theory is used in agreement with the experimental results: α is a complex wavenumber and ω is real. The local amplification of the instability wave is given by $-\alpha_i$, the negative of the imaginary part of α , whereas the wavenumber and the frequency are given by α_r , the real part of α , and by $\omega/2\pi$ (the dimensional frequency is $\omega V_{inj}/(2\pi a)$). Finally, q representing the azimuthal wavenumber is an integer.

The use of local theories is based on the ‘quasi-parallel approximation’, i.e. on the assumption that the mean flow varies weakly with x over an instability wavelength. Consequently only modes which have a sufficiently short wavelength can be kept.

Contrary to the LNP approach, the strictly parallel theory seems to give wrong results if we compare its results in *figure 3* with the PSE calculations which take into account the nonparallel effects. The same remark had been made in the planar case and we can notice that *figure 3* looks like *figure 11* in [6]. Thus we use the LNP approach and keep the terms \bar{U}_r and $\partial\bar{U}_x/\partial x$ even if the approach is not strictly consistent.

3.2. Stability equations

The linearised Navier–Stokes equations can be transformed into a first order differential system

$$\frac{d\vec{Z}(r)}{dr} = \mathcal{L}\vec{Z}(r) \quad (6)$$

for the unknown vector of dimension six:

$$\vec{Z}(r) = \left(\hat{u}_x(r), \hat{u}_r(r), \hat{u}_\theta(r), \hat{p}(r), \frac{d\hat{u}_x}{dr}(r), \frac{d\hat{u}_\theta}{dr}(r) \right). \quad (7)$$

In the system (6), \mathcal{L} is a linear operator depending on α , ω , q , \mathcal{R}_{inj} and on the mean flow. Its coefficients are given in Appendix A.

The boundary conditions become:

$$\hat{u}_x(1) = \hat{u}_r(1) = \hat{u}_\theta(1) = 0. \quad (8)$$

3.3. Eigenvalue problem

Since the system comprised of equations (6) and boundary conditions (8) is homogeneous, it is satisfied by the trivial solution. To admit a nontrivial solution, the problem must be singular. So we have to solve an eigenvalue problem with an implicit dispersion relation between the parameters:

$$\mathcal{F}(\alpha, \omega, q, x, \mathcal{R}_{\text{inj}}) = 0. \quad (9)$$

This relation is solved numerically, see next section, by fixing $\omega, q, x, \mathcal{R}_{\text{inj}}$, so that (9) provides the admissible complex wavenumbers α . Then the amplitude A of the perturbation is obtained by integrating the local amplification of the wave. For fixed values of \mathcal{R}_{inj} and q , the amplitude is given by:

$$A(x, \omega) = A_0 e^n \quad \text{with } n(x, \omega) = \int_{x_0(\omega)}^x -\alpha_i(\xi, \omega) d\xi. \quad (10)$$

As it is done in the framework of the boundary layer stability theory, see [11], $x_0(\omega)$ is the first axial position where the marginal stability is reached. Although the initial amplitude A_0 may depend on ω , nothing is known about this dependence, so it is actually assumed to be independent of the frequency. Since the theory is linear, this multiplicative constant is definitely unknown.

4. Numerical procedure

The problem is constituted by the system (6) of order six, associated with the three boundary conditions (8).

Hence, three conditions seem to be missing. Indeed, the singularity of the equations at the axis, $r = 0$, induced by the choice of the cylindrical coordinates leads to three ‘compatibility’ relations. By expressing that the singularity is not physical but due to the choice of the coordinates, so that the physical quantities have finite values and can be expanded in power series near the axis, three additional conditions can be found. The whole problem hence becomes well-posed.

Thus, the numerical procedure needs a special treatment near the axis. Below a critical radius r_c , the known steady flow quantities and the unknown functions, which have finite values in the whole channel, are written in the form of Taylor series expansions. These expansions are introduced into the system (6). As shown in Appendix B, all the coefficients can be found as functions of three arbitrary ones, corresponding to the three physical boundary conditions at the wall which are not taken into account in the expansion close to the axis.

In the domain $r \leq r_c$, the six components of vector \vec{Z} are calculated as a function of three arbitrary coefficients, say a_c, b_c, c_c . Furthermore, as demonstrated in Appendix B, the dependence with respect to these coefficients is linear, so we can write:

$$\vec{Z}(r) = a_c \vec{F}(r) + b_c \vec{G}(r) + c_c \vec{H}(r). \quad (11)$$

This form represents six scalar equations in which the elimination of the three unknown constants a_c, b_c, c_c leads to three compatibility relations, linearly independent, between the coefficients of $\vec{Z}(r)$. These three conditions are written at $r = r_c$.

We have used Taylor series expansions of order as high as 20 in the vicinity of $r = 0$ but we found that the first two nonzero terms (their order depends on q) of each unknown function give the same result as higher order if r_c remains small and if the grid contains enough points.

For $r \in [r_c, 1]$, the system (6) of order six with the three compatibility conditions at r_c and the three conditions at the wall is solved with a subroutine which has been developed for solutions of boundary layer stability problems, see [12]. The numerical scheme is a fourth order compact scheme presented in [13]. Finally, for fixed values of $\alpha, \omega, x, q, \mathcal{R}_{inj}$ the equations (6) can be integrated.

To solve the eigenvalue problem, the values of ω, x, q are fixed and α is searched so that the operator is singular. Our method consists in modifying the boundary conditions as, for example:

$$\hat{u}_x(1) = \hat{u}_\theta(1) = 0 \quad \text{and} \quad \hat{p}(1) = 1$$

(so that the trivial solution does not satisfy the boundary conditions), and in iterating the integrations of (6) with a Newton–Raphson procedure on α until the physical boundary condition $\hat{u}_r(1) = 0$ is satisfied.

The relation $\hat{p}(1) = 1$ acts as a normalization. In the results which are presented in this paper, the eigenfunctions are generally related together with this normalization.

The whole procedure has been validated in the well-known case of the stability of the pipe-Poiseuille flow. For instance, comparisons have been made with the results of Garg et al. [14], Khorrami et al. [15] and Tumin [16], see *tables I* and *II* for two- and three-dimensional modes. Excellent agreement is clearly obtained.

Table I. Most unstable eigenvalue of the cylindrical Poiseuille flow for $q = 0, \mathcal{R}_e = 10000, \omega = 0.5$.

Results of	Re(α)	Im(α)
Garg and Rouleau [14]	0.51998925173	0.02083549388
Khorrami et al. [15]	0.51998925171	0.02083549388
Tumin [16]	0.51998925173	0.02083549388
Present computations	0.51998925173	0.02083549388

Table II. Eigenvalues of the cylindrical Poiseuille flow for $q = 0, 1, 2$ and $3, \mathcal{R}_e = 2280, \omega = 0.96$.

Tumin [16]		Present computations	
Re(α)	Im(α)	Re(α)	Im(α)
$q = 1$			
1.0635965	0.05122505	1.063596491	0.0512250545
1.466419	0.61187152	1.46641951	0.61187122
$q = 2$			
1.091291	0.07696552	1.09129126	0.076965517
1.3004755	0.71352031	1.3004755	0.71352051
$q = 3$			
1.119773	0.10921440	1.11977346	0.109214397
1.3182548	0.76810573	1.31825481	0.76810600

5. Results

The described procedure provides different eigenmodes. For each fixed value of q , more than one mode can be found but some of them are stable or do not seem physically acceptable. So only one mode has been retained in each case. For instance, for $\omega = 80$, $x = 10$, $q = 0$, $\mathcal{R}_{inj} = 4500$, we take only into account the most unstable of the four eigenvalues which are given in *table III*.

The graph of the iso- n factor computed from equation (10), see *figure 4* for $q = 0$, gives a good idea of the spatial amplification of the flow. The curve plotted with a thick line is the neutral curve, i.e. the location where the waves become marginally stable; they are amplified downstream. Some observations may be made. First, near the headwall, the mean flow is linearly stable. The critical value for $\mathcal{R}_{inj} = 4000$ and $q = 0$ is:

$$x = 3.18335487, \quad \omega = 39.76431, \quad \alpha_r = 5.49430685, \quad \alpha_i = 0.$$

Then one can observe that the neutral curve never reaches some low frequencies, which are always damped. At a given x -location, the frequencies inside the neutral curve show the range of the amplified frequencies. Finally, with the definition

$$n_{\max}(x) = \max_{\omega \in \mathbb{R}^+} \{n(x, \omega)\} \quad (12)$$

it can be seen from the curve of $n_{\max}(x)$ in *figure 4* that the most amplified frequency increases almost linearly as the flow approaches the exhaust of the channel.

The corresponding wavelengths are plotted in *figure 5*. As usual, the modes with low frequencies have a longer wavelength than modes with higher frequencies. On the other hand for fixed ω , the wavelength increases with increasing axial position. Finally it may be important to note that the dimensional wavelength of the most amplified wave is of the order of the radius of the channel.

As noticed in the planar case, see [6], the effect of the Reynolds number on the stability results is very weak as soon as the Reynolds number reaches one thousand, as is apparent in *figure 2*. This remark will be useful for the interpretation of the experimental results.

For $q = 0$ the perturbation is two-dimensional, however three-dimensional perturbations can be found too. *Figure 6* compares the neutral curves for $q = 0, 1, 2, 3$. It can be seen that the ranges of amplified frequencies are not very different from one mode to the other, except for low frequencies, so that it will be difficult to isolate them among the experimental results. Furthermore, the curve of n_{\max} shows that the most amplified frequencies have the same evolution with x .

Examples of eigenfunctions are given on the right part of *figure 8*. The shape of the eigenfunction for $q = 0$ is similar to the one for the planar configuration, see *figure 4* in [6]. The main feature consists in a maximum of the streamwise velocity component located close to the wall. For higher azimuthal wavenumber, other maxima occur, see for example $q = 3$ in *figure 8*.

Table III. Eigenvalues of the cylindrical Taylor flow for $\omega = 80$, $x = 10$, $q = 0$, $\mathcal{R}_{inj} = 4500$.

	α_r	α_i
Mode 1	6.0952945656	-1.0787998140
Mode 2	3.3264285366	-0.1095525589
Mode 3	2.6013223310	0.1322870315
Mode 4	2.4160703725	0.3731054183

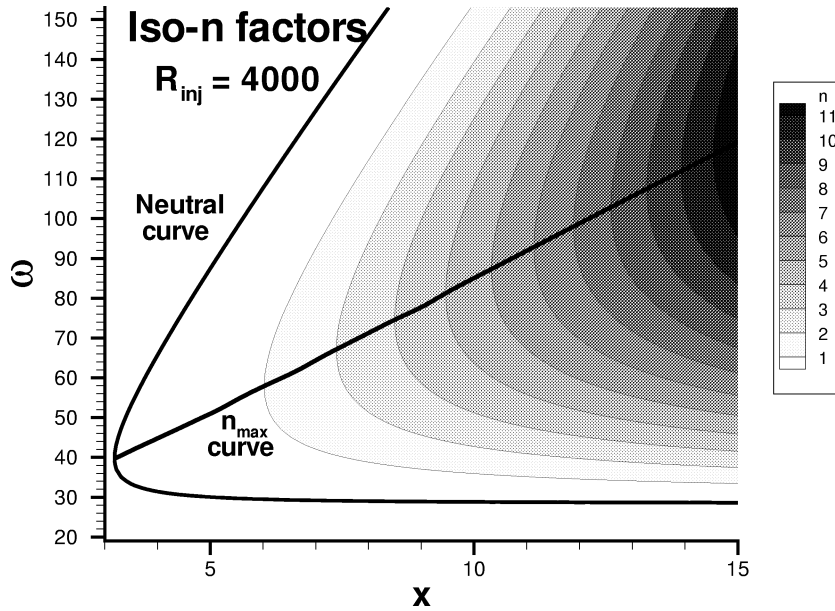


Figure 4. Neutral curve, iso- n factors and curve of n_{max} , the maximum n factor of the bidimensional mode $q = 0$ for $R_{inj} = 4000$.

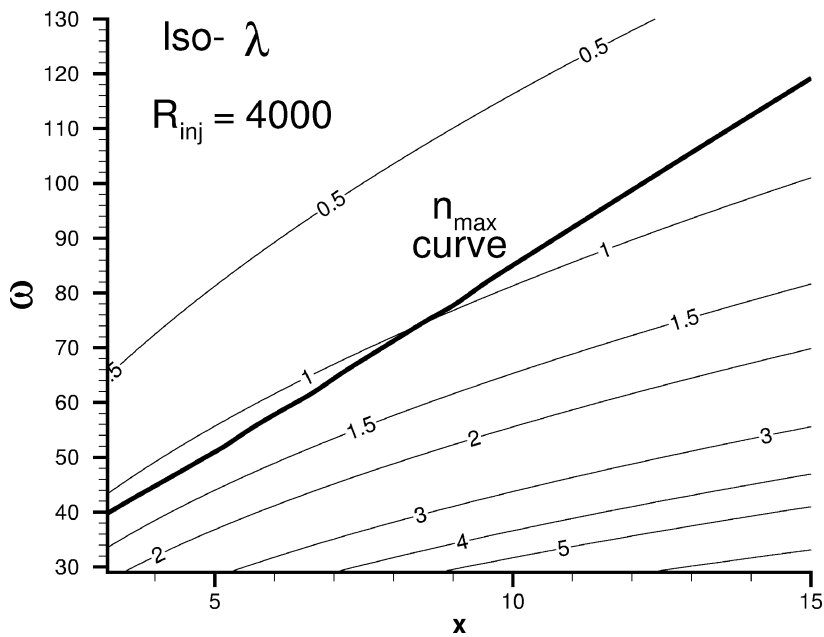


Figure 5. Iso-values of the wavelength $\lambda = 2\pi/\alpha_r$ and curve of n_{max} , the maximum n factor of the bidimensional mode $q = 0$ for $R_{inj} = 4000$.

6. Comparison with the experimental results

In order to estimate the validity of our approach, we tried to compare our theoretical results with the experimental ones published by Dunlap et al. in [8] who used a facility corresponding to the geometry of our

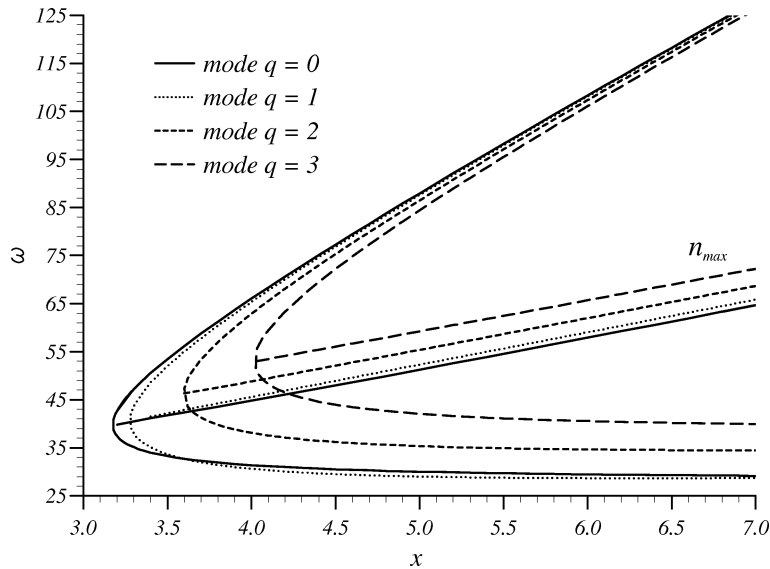


Figure 6. Neutral curves and curves of n_{\max} , the maximum n factor of modes for azimuthal wavenumber $q \in \{0, 1, 2, 3\}$. $\mathcal{R}_{\text{inj}} = 4500$.

Table IV. Experimental configurations of the cold-flow set-up presented by Dunlap et al. [8] which are used for comparisons.

	M_w	L/D
Case 1	0.0018	14.3
Case 2	0.0027	9.5
Case 3	0.0036	14.3

study. This article provides data concerning the mean flow which is, as expected, close to the Taylor solution except close to the axis where some swirl is observed.

Measurements of fluctuations are also made. We will first present the three kinds of data which are available: spectra, radial shape and streamwise evolution of the fluctuation. We will then make comparisons with the theoretical predictions for each kind of results.

It must be pointed out that the experiments were not performed in a framework of a stability study so that most of the measurements cannot be directly compared to our results, as we will explain in the next subsection. Furthermore, the possible occurrence of acoustic resonance is not clear and we know [7] that this may strongly affect the unsteady flow field.

Consequently, we cannot exhibit a clear proof of the validity of our approach but we will show that no contradiction has been found whereas a qualitative agreement is often obtained. Therefore, the occurrence of the intrinsic instability mechanisms, even if not accurately predicted, seems to be confirmed.

6.1. Available results

Experiments in [8] have been performed for three combinations of injection Mach number M_w and ratio of length to diameter L/D (but with the same diameter): $M_w = 0.0018$ and $L/D = 14.3$ (case 1), $M_w = 0.0027$ and $L/D = 9.5$ (case 2), and $M_w = 0.0036$ and $L/D = 14.3$ (case 3), see *table IV*. In each case, the axial, radial and circumferential fluctuations are plotted at several x -locations versus the radius but the precision of the plots

does not allow accurate comparisons of the spatial growth of the instability wave. At the nondimensionalised abscissa $x = 10.92$, axial velocity spectra are plotted for three different distances from the porous wall.

The main difficulty for the comparison is the measurement of the fluctuation: the theory predicts the behaviour of isolated waves corresponding to one frequency, whereas the experimental signal proceeds from hot wire measurements, which are integrated over a large frequency range. Only the spectra can be directly compared with our results.

Furthermore, for each frequency, all the measurements give probably a combination of azimuthal modes but it is difficult to know which azimuthal modes are really present in the flow and which initial amplitude they have. Hence, the comparison is not easy.

6.2. About re-scaling

It must be pointed out that the three considered test cases correspond only to one stability calculation for the following reasons. First, we analyse the stability of the Taylor flow which is strictly a solution of the Euler equations and which is only valid for a semiinfinite cylinder, so that the downstream extremity of the channel is not taken into account by our theory. This means that theoretically there is no difference between cases 1 and 3. Secondly, after nondimensionalisation, the differences due to the three injection Mach numbers result only in a range of Reynolds numbers from 4.5×10^3 to 9×10^3 . But as mentioned above, in this range, the stability results are almost independent of the Reynolds number, see *figure 2*. Moreover, the plots are given at the same nondimensionalised x -location, so we just need one computation at $\mathcal{R}_{\text{inj}} = 4.5 \times 10^3$ and we obtain the three cases by re-scaling.

The radius a is $a = 5.1$ cm. For the injection velocity, the wall Mach number is given (see *table IV*) and we know that the experiments were performed with nitrogen at approximately 0.21 MPa with an average temperature varying over the range -16 to $+13^\circ\text{C}$, so we choose the velocity of sound $c = 340$ m s $^{-1}$.

6.3. Comparison of the spectra

Spectra are given at the nondimensionalised abscissa $x = 10.92$. For each azimuthal mode q , the computation of the n -factors at this abscissa leads to the function $n(\omega)$. Then the spectra are provided in terms of the physical frequency $f^* = \omega V_{\text{inj}} / (2\pi a)$ by

$$S(f^*) = (A_0 e^{n(f^*)})^2.$$

Since the channel radius used for the three spectra is the same, the theory predicts that the amplified dimensional frequencies are proportional to the injection velocity. Measurements not too close to the wall (spectra close to the wall seem to be modified by nonlinear phenomena, as discussed later, so they are not directly useful) confirm this expectation: for a wall Mach number $M_w = V_{\text{inj}}/c = 0.0018$ the most amplified frequency is 140 Hz, it is around 230 Hz for $M_w = 0.0027$ and 280 Hz for $M_w = 0.0036$. The frequency of case 2 for which the channel has a shorter length is not exactly proportional. Does this length affect the intensity of the swirl close to the axis? Are some acoustic effects present?

The comparison of the experimental spectrum of case 1 with the theoretical amplitude for different azimuthal modes q is given in *figure 7*. Since the constant A_0 is unknown, the absolute value of the amplitude has no meaning. Furthermore, the figure is plotted with the same constant A_0 for each q -mode.

For case 1, *figure 7* indicates a shift of frequency of almost 35 Hz (25%) between the experimental value of the most amplified frequency $f^* = 140$ Hz and the theoretical one for $q = 0$ (175 Hz). This shift grows very

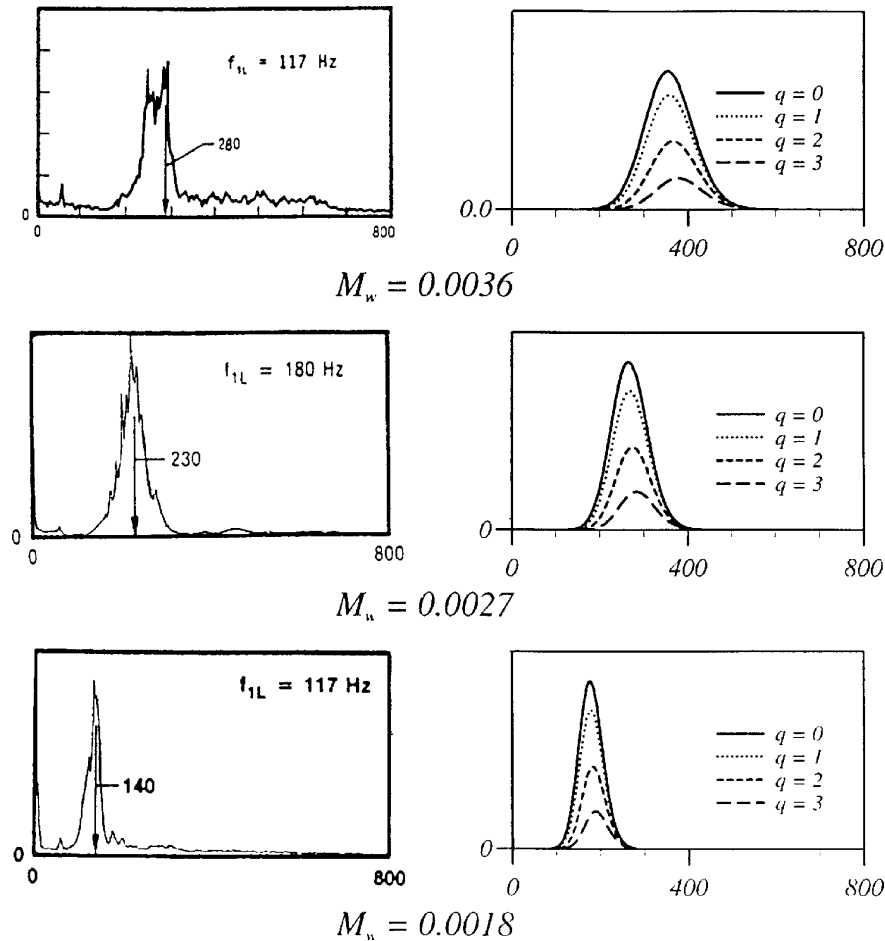


Figure 7. Comparison between experimental and theoretical spectra of the square of the axial fluctuation for $x = 10.92$ and $r = 0.75$ ($r = 1$ corresponds to the porous wall) for three injection Mach numbers. Only the frequencies are dimensionalised (in Hz).

weakly with q . Many explanations for this shift are possible: the small swirl phenomenon present near the axis, the influence of the acoustics, imprecisions in the sound speed and in the Mach number, etc. Furthermore, the theoretical range of amplified frequencies is a bit thicker than the experimental one.

As predicted, the two other comparisons for cases 2 and 3 lead to the same conclusions. It must be emphasized that the spectra exhibit a bump of amplified frequencies, as predicted by an instability mechanism and that they do not exhibit peaks as would be expected by an acoustic phenomenon. The results are therefore qualitatively encouraging.

6.4. Axial, radial and circumferential eigenfunctions

Again at the location $x = 10.92$, the authors of [8] give the axial rms velocity fluctuations. As explained before, the measured velocity fluctuations are not given for one frequency (or a small frequency band) but for a large (unknown) frequency range. Furthermore, for each frequency, it is not possible to distinguish experimentally the azimuthal modes. But although all the frequencies and azimuthal modes are present in the graphs of velocity fluctuations, we can try to compare them with the eigenfunctions of the most amplified

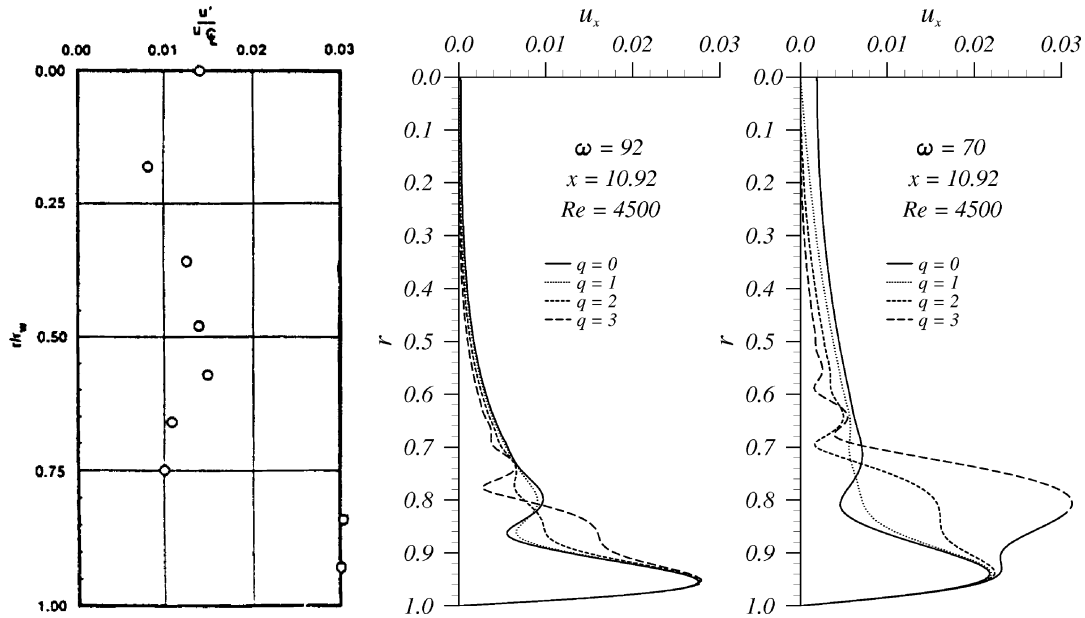


Figure 8. Comparison between the experimental rms axial velocity fluctuations profile (fraction of the axial centerline velocity versus nondimensionalised radius) and theoretical axial eigenfunctions for the most amplified frequency corresponding to $\omega = 92$ and for a less amplified frequency corresponding to $\omega = 70$. $x = 10.92$, $Re_{inj} = 4500$, $M_w = 0.0018$ (case 1).

frequencies of each q mode. We plot the eigenfunction $\vec{\hat{u}}(r)$ and not $A_0\vec{\hat{u}}(r)e^n$ and we choose the normalization $\hat{p}(1) = 0.15$ so that the amplitude of the eigenfunction $\hat{u}_x(r)$ of the mode $\omega = 92$, $q = 0$ matches the rms fluctuation. Of course we use the same normalization for all the eigenfunctions of figures 8 and 9.

First, the main feature of the eigenfunctions seems to appear on the graphs of the rms axial, radial and circumferential velocity fluctuations given in figures 8 and 9: a maximum of high amplitude near the wall.

Secondly, the experimental and theoretical ratio of the amplitudes of axial, radial and circumferential fluctuations, which are independent of the normalization for fixed ω, q , agree quite well.

Third, as explained in Section 6.2, the velocity fluctuations should have the same shape in the three cases (only the initial amplitude A_0 can change). This is well confirmed for the three cases.

Finally, Dunlap et al. [8] notice at section $x = 10.92$ a phenomenon which cannot be explained by the present linear theory. For cases 1 and 3 the most amplified frequency (f_{max}^{wall}) measured close to the wall ($r \approx 0.9$) is twice what it is (f_{max}^{cl}) in the rest of the x -section ($r \leq 0.75$), i.e. $f_{max}^{wall} = 2f_{max}^{cl}$. Nonlinear phenomena can be suspected in so far as the amplitudes for cases 1 and 3 are very large close to the wall (3% of the centerline mean velocity).

6.5. Spatial amplification

Figures 8–10 and 16–18 of the article [8] have to be discussed too. The normal mode form (5) implies that longitudinal, radial and circumferential components of the velocity fluctuations have the same exponential evolution with respect to x in the linear domain. To confirm this, we look at the closest points to the wall (where the instability wave has the largest amplitude and can be distinguished from the environmental noise). We plot in figure 10 the x -evolution for case 3 of the fluctuations at $r = 0.95$ extracted from the published figures in [8].

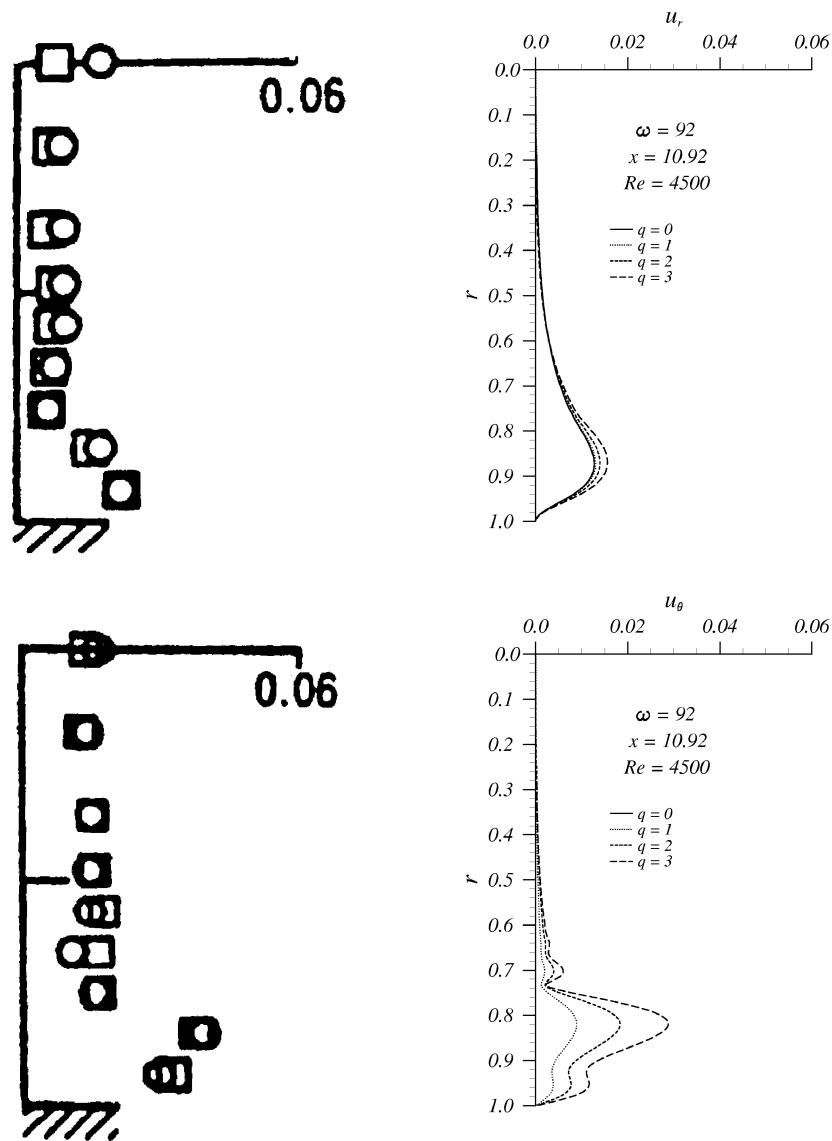


Figure 9. Comparison between the experimental rms radial and rms circumferential velocity fluctuations profiles (fraction of the axial centerline velocity versus nondimensionalised radius) and the radial and circumferential eigenfunctions for the most amplified frequency corresponding to $\omega = 92$ for $x = 10.92$. The circular symbols of experimental results are obtained for $M_w = 0.0018$ (case 1) whereas the square ones correspond to $M_w = 0.0036$ (case 3).

First, it is clear that longitudinal, radial and circumferential components of the velocity fluctuation behave the same way from different initial amplitudes.

As before, fluctuations are obtained by an integration over the frequencies and the azimuthal modes. However, the spatial amplification of the most amplified frequency (which changes with x) for $q = 0$ may be representative. So we plot $A_0 \exp(n_{\max}(x))/x$ (see equation (12)) in figure 10 with $A_0 = 1/2000$ (we divide $\exp(n_{\max})$ by x because the velocities are nondimensionalised with the axial centerline velocity in [8]). It must be pointed out that the measurements give not only the eigenresponse but also fluctuations which are not instability eigenmodes. The theoretical results exhibit a very rapid and large amplification which is most likely

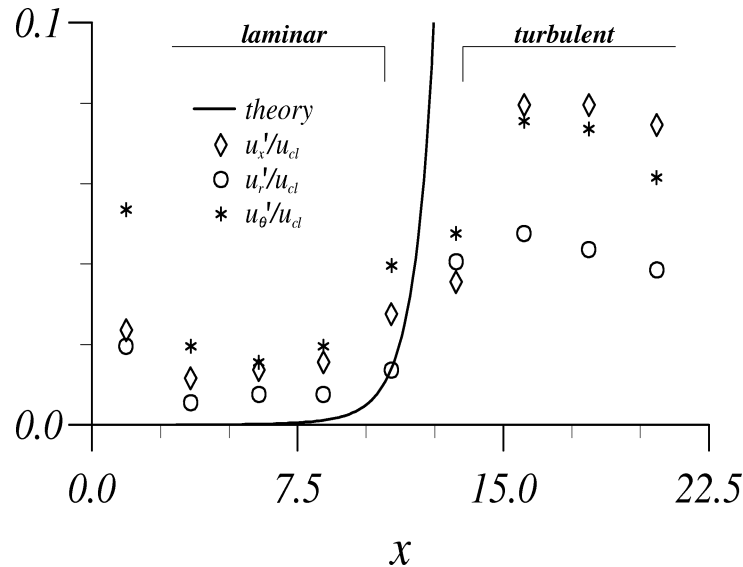


Figure 10. Experimental spatial evolution of the ratio of the fluctuation amplitude to the centerline axial velocity for $M_w = 0.0036$ (case 3) and $r = 0.95$. Comparison with $(1/2000)\exp(n_{\max}(x))/x$ for $q = 0$. For $x \leq 10.92$, the flow is laminar whereas for $x \geq 13.28$, it is turbulent.

related to the laminar-turbulent transition since measurements [8] show that the flow is laminar for $x \leq 10.92$ and turbulent for $x \geq 13.28$.

The experimental results plotted in *figure 10* seem to indicate that some instability modes are present close to the headwall and that they decay in x up to a location which is in the vicinity of the theoretical neutral curve. However, additional comparisons with the theory may be not relevant due to our assumption $A_0(x, \omega) = \text{constant}$.

Finally, the agreement between theory and experiment is not striking but the linear domain where the exponential law could have been validated is short and the beginning of the amplification seems correctly predicted.

7. Summary

The study consists in a local linear stability analysis applied to the nonparallel incompressible flow induced by wall injection in a cylindrical channel. The quasi-parallel approximation is assumed but some terms remain in the final stability equations, such as the radial mean velocity, which would have been neglected in a strictly consistent approach. However, the comparison with nonlocal calculations proved as in [6] that these terms must be kept to provide good results.

The problem to solve is an eigenvalue problem with an implicit dispersion relation between the axial wavenumber, the local axial amplification, the frequency, the azimuthal wavenumber, the Reynolds number and the streamwise coordinate x through the similarity solution for the base flow. The integration of the system of stability equations is required to compute the dispersion relation but it needs a particular treatment near the axis due to the choice of the cylindrical coordinates.

The analysis shows that the flow is stable near the headwall until it reaches a critical axial distance from the headwall nondimensionalized with the radius a of almost 3.2 for a dimensionless pulsation close to 40 (nondimensionalized with the injection velocity divided by the radius V_{inj}/a) and a Reynolds number of order

4000 and becomes unstable downstream. This first instability occurs for a two-dimensional mode but our results show that three-dimensional modes may be also amplified, at least for low values of the azimuthal wavenumber.

Comparisons have been made with some available experimental results published by Dunlap et al. [8]. The comparisons of the spectra agree quite well, when a shift in frequency is taken into account. The main features of the eigenfunctions and of the spatial amplification seem to be the same as the theoretical predictions. Therefore, it can be assumed that intrinsic instability mechanisms are really present in axisymmetric problems and explain the experimental flow behaviour as they do in the case of planar ducts, see [6].

These instability mechanisms, as seen in [6], seem to provide possible sources of acoustic energy in porous-walled ducts. This phenomenon may be therefore useful to understand oscillatory behaviour of the flow inside solid propellant motors.

Appendix A

As explained in Section 3.2, the linear stability equations can be written:

$$\frac{d\vec{Z}}{dr} = \mathcal{L}\vec{Z}, \quad \vec{Z} = \left(\hat{u}_x, \hat{u}_r, \hat{u}_\theta, \hat{p}, \frac{d\hat{u}_x}{dr}, \frac{d\hat{u}_\theta}{dr} \right),$$

where

$$\mathcal{L} = \begin{bmatrix} 0 & 0 & 0 & 0 & 1 & 0 \\ \mathcal{L}_{21} & \mathcal{L}_{22} & \mathcal{L}_{23} & 0 & 0 & 0 \\ 0 & 0 & 0 & 0 & 0 & 1 \\ \mathcal{L}_{41} & \mathcal{L}_{42} & \mathcal{L}_{43} & 0 & \mathcal{L}_{45} & \mathcal{L}_{46} \\ \mathcal{L}_{51} & \mathcal{L}_{52} & 0 & \mathcal{L}_{54} & \mathcal{L}_{55} & 0 \\ 0 & \mathcal{L}_{62} & \mathcal{L}_{63} & \mathcal{L}_{64} & 0 & \mathcal{L}_{66} \end{bmatrix}, \quad (13)$$

$$\begin{aligned} \mathcal{L}_{21} &= -i\alpha, & \mathcal{L}_{22} &= -\frac{1}{r}, & \mathcal{L}_{23} &= -\frac{iq}{r}, \\ \mathcal{L}_{41} &= \overline{U}_r i\alpha, & \mathcal{L}_{42} &= -\frac{\gamma'}{\mathcal{R}_{inj}} - \frac{\partial \overline{U}_r}{\partial r} + \frac{\overline{U}_r}{r}, & \mathcal{L}_{43} &= -\frac{iq}{\mathcal{R}_{inj} r^2} + \overline{U}_r \frac{iq}{r}, \\ \mathcal{L}_{45} &= -\frac{i\alpha}{\mathcal{R}_{inj}}, & \mathcal{L}_{46} &= -\frac{iq}{\mathcal{R}_{inj} r}, \\ \mathcal{L}_{51} &= \gamma' + \mathcal{R}_{inj} \frac{\partial \overline{U}_x}{\partial x}, & \mathcal{L}_{52} &= \mathcal{R}_{inj} \frac{\partial \overline{U}_x}{\partial r}, & \mathcal{L}_{54} &= \mathcal{R}_{inj} i\alpha, & \mathcal{L}_{55} &= \mathcal{R}_{inj} \overline{U}_r - \frac{1}{r}, \\ \mathcal{L}_{62} &= -\frac{2iq}{r^2}, & \mathcal{L}_{63} &= \gamma' + \frac{1}{r^2} + \frac{\mathcal{R}_{inj} \overline{U}_r}{r}, & \mathcal{L}_{64} &= \frac{\mathcal{R}_{inj} iq}{r}, & \mathcal{L}_{66} &= \mathcal{R}_{inj} \overline{U}_r - \frac{1}{r}, \end{aligned} \quad (14)$$

with $\gamma' = \alpha^2 + q^2/r^2 + \mathcal{R}_{inj} i(\alpha \overline{U}_x - \omega)$.

Appendix B

The detail of the treatment of the central axis is the following. The unknown functions are written in the form of a Taylor series expansion

$$\begin{cases} \hat{u}_x = \sum_{n=0}^{\infty} u_n r^n, \\ \hat{u}_r = \sum_{n=0}^{\infty} v_n r^n, \\ \hat{u}_\theta = \sum_{n=0}^{\infty} w_n r^n, \\ \hat{p} = \sum_{n=0}^{\infty} p_n r^n. \end{cases} \quad (15)$$

Likewise, the known steady flow is expanded as

$$\begin{cases} \bar{U}_x = f(x) \sum_{n=0}^{\infty} A_n r^n, \\ \bar{U}_r = \sum_{n=0}^{\infty} B_n r^n, \\ \bar{U}_\theta = 0. \end{cases} \quad (16)$$

(These expressions can be used for Poiseuille and Taylor flows.)

The expansions are introduced in (6). For each order, the four equations obtained from (6) can be written:

- System S_0 :

$$\begin{cases} -q^2 u_0 = 0, \\ v_0 + i q w_0 = 0, \\ -(1 + q^2) v_0 - 2 i q w_0 = 0, \\ 2 i q v_0 - (1 + q^2) w_0 = 0. \end{cases} \quad (17)$$

- System S_1 :

$$\begin{cases} (1 - q^2) u_1 = 0, \\ 2 v_1 + i q w_1 = -i \alpha u_0, \\ -q^2 v_1 - 2 i q w_1 = 0, \\ 2 i q v_1 - q^2 w_1 - \mathcal{R}_{inj} i q p_0 = \mathcal{R}_{inj} w_0 B_0. \end{cases} \quad (18)$$

- System S_{n+2} , for all $n \geq 0$:

$$\begin{cases} (\alpha^2 - i \mathcal{R}_{inj} \omega) u_n + i \mathcal{R}_{inj} \alpha p_n + \mathcal{R}_{inj} \sum_{j=0}^n ((f'(x) + i \alpha f(x)) A_j u_{n-j} \\ \quad + (n + 1 - j) B_j u_{n+1-j} + f(x)(j + 1) v_{n-j} A_{j+1}) = ((n + 2)^2 - q^2) u_{n+2}, \\ (n + 3) v_{n+2} + i q w_{n+2} = -i \alpha u_{n+1}, \\ ((n + 2)^2 - (1 + q^2)) v_{n+2} - 2 i q w_{n+2} - \mathcal{R}_{inj} (n + 1) p_{n+1} = \mathcal{R}_{inj} ((\frac{\alpha^2}{\mathcal{R}_{inj}} - i \omega) v_n \\ \quad + \sum_{j=0}^n (i \alpha f(x) A_j v_{n-j} + (n + 1) B_j v_{n+1-j}) + (n + 1) v_0 B_{n+1}), \\ 2 i q v_{n+2} + ((n + 2)^2 - (1 + q^2)) w_{n+2} - \mathcal{R}_{inj} i q p_{n+1} = \mathcal{R}_{inj} ((\frac{\alpha^2}{\mathcal{R}_{inj}} - i \omega) w_n \\ \quad + \sum_{j=0}^n (i \alpha f(x) A_j w_{n-j} + (n + 2 - j) B_j w_{n+1-j}) + w_0 B_{n+1}). \end{cases} \quad (19)$$

Some remarks can be made about these systems:

- Each S_i system contains the coefficients u_i , v_i , w_i and p_{i-1} and others of lower order. So each S_i gives u_i , v_i , w_i and p_{i-1} .
- The system obtained from (19) with the unknown coefficients (u_i , v_i , w_i and p_{i-1}) has a determinant of value of

$$\Delta = (i^2 - q^2)(i^2 - (q + 1)^2)(i^2 - (q - 1)^2)$$

which implies that whatever be the azimuthal wavenumber q the system becomes singular for three orders. This shows that the whole problem constituted by the expansions is singular. Systems S_i are degenerated of order 1 at three orders so that three coefficients of the expansion remain necessarily arbitrary. Indeed, the three physical conditions are given at the wall and are not used in the expansion near the axis. So it is consistent that three coefficients of the development take arbitrary values.

With q as a parameter, calculations give:

- $q = 0$
 - * (17) $\Rightarrow u_0$ is arbitrary, $v_0 = w_0 = 0$.
 - * (18) $\Rightarrow u_1 = 0$, p_0 and w_1 are arbitrary and $v_1 = -i\alpha u_0/2$.
 - * $\forall n \geq 0$: u_{n+2} , v_{n+2} , w_{n+2} and p_{n+1} are solutions of (19).
- $q = 1$
 - * (17) $\Rightarrow u_0 = 0$, v_0 and w_0 are related by $v_0 + iq w_0 = 0$: v_0 or w_0 is arbitrary.
 - * (18) $\Rightarrow u_1$ is arbitrary, $v_1 = w_1 = 0$, p_0 satisfies $p_0 = i w_0 B_0$.
 - * (19) for $n = 0 \Rightarrow u_2$ is given by the first equation, p_1 is arbitrary, v_2 and w_2 are related by:

$$\begin{cases} 5v_2 + iw_2 = -i\alpha u_1, \\ 2v_2 - 2iw_2 = \mathcal{R}_{\text{inj}} \left[\left(\frac{\alpha^2}{\mathcal{R}_{\text{inj}}} - i\omega \right) v_0 + v_0 B_1 \right]. \end{cases} \quad (20)$$

- * $\forall n \geq 1$: u_{n+2} , v_{n+2} , w_{n+2} and p_{n+1} are solutions of (19).
- $q \geq 2$
 - * $\forall n$, $n + 2 \leq q - 2$: $u_{n+2} = v_{n+2} = w_{n+2} = 0$ and $p_{n+1} = 0$.
 - * $u_{q-1} = 0$ and $p_{q-2} = 0$; v_{q-1} and w_{q-1} are related by $v_{q-1} + iq w_{q-1} = 0$: v_{q-1} or w_{q-1} is arbitrary.
 - * u_q is arbitrary, $v_q = w_q = 0$, p_{q-1} satisfies $p_{q-1} = i w_0 B_{q-1}$.
 - * u_{q+1} is given by the first equation of (19), p_q is arbitrary, v_{q+1} and w_{q+1} are related by:

$$\begin{cases} (q + 4)v_{q+1} + iq w_{q+1} = -i\alpha u_q, \\ 2qv_{q+1} - 2iq w_{q+1} = \mathcal{R}_{\text{inj}} \left(\left(\frac{\alpha^2}{\mathcal{R}_{\text{inj}}} - i\omega \right) v_{q-1} + \sum_{j=0}^{q-1} (i\alpha f(x) A_j v_{q-1-j} + q B_j v_{q-j}) + q v_0 B_q \right). \end{cases} \quad (21)$$

- * $\forall n$, $n + 2 \geq q + 2$: u_{n+2} , v_{n+2} , w_{n+2} and p_{n+1} are solutions of (19).

Finally, as predicted, three coefficients remain arbitrary in any case. Furthermore, all the coefficients linearly depend on the vector constituted by the three arbitrary constants.

Acknowledgements

This study has been performed in the framework of the research program ‘‘Aerodynamics of Segmented Solid Motors’’ conducted and supported by the Centre National d’Etudes Spatiales (CNES) and coordinated by the

Office National d'Etudes et de Recherches Aéronautiques (ONERA). This program involves the participation of industrial companies/partners, and university laboratories.

References

- [1] Brown R.S., Dunlap R., Young S.W., Waugh R.C., Vortex shedding as a source of acoustic energy in segmented solid rockets, *J. Spacecraft* 18 (4) 1981.
- [2] Avalon G., Comas P., Simulative study of the unsteady flow inside a solid propellant rocket motor, in: 27th Joint Propulsion Conference and Exhibit, AIAA/ASEE/ASME/SAE, AIAA Paper 91-1866, Sacramento, CA, June 24–26, 1991.
- [3] Lupoglazoff N., Vuillot F., Numerical simulations of parietal vortex-shedding phenomenon in a cold flow set-up, in: Joint Propulsion Conference and Exhibit, AIAA/ASME/ASEE, Cleveland, OH, July 13–15, 1998.
- [4] Varapaev V.N., Yagodkin V.I., Flow stability in a channel with porous wall, *Izv. AN SSSR. Mekhanika Zhidkosi i Gaza* 4 (5) (1969).
- [5] Lupoglazoff N., Vuillot F., Parietal vortex shedding as a cause of instability for long solid propellant motors. Numerical simulations and comparisons with firing tests, AIAA Paper 96-0761, 1996.
- [6] Casalis G., Avalon G., Pineau J.P., Spatial instability of planar channel flow with fluid injection through porous walls, *Phys. Fluid* 10 (10) (1998) 2558–2568.
- [7] Avalon G., Casalis G., Griffond J., Flow instabilities and acoustic resonance of channels with wall injection, in: Joint Propulsion Conference and Exhibit, AIAA/ASME/ASEE, Cleveland OH, July 13–15, 1998.
- [8] Dunlap R., Blackner A.M., Waugh R.C., Brown R.S., Willoughby P.G., Internal flow field studies in a simulated cylindrical port rocket chamber, *J. Propul. Power* 6 (6) (1990).
- [9] Taylor G.I., Fluid flow in regions bounded by porous surfaces, *P. Roy. Soc. Lond. A Math.* 234 (1199) (1956) 456–475.
- [10] Herbert T., Bertolotti F.P., Stability analysis of non-parallel boundary layers, *B. Am. Phys. Soc.* 32 (1987).
- [11] Arnal D., Boundary layer transition: prediction based on linear stability theory, AGARD REPORT, 793, 1994.
- [12] Airiau C., Stabilité linéaire et faiblement non-linéaire d'une couche limite incompressible par un système d'équations parabolisé (PSE), PhD thesis, ENSAE, Toulouse, June 1994.
- [13] Malik M.R., Chuang S., Hussaini M.Y., Accurate numerical solution of compressible, linear stability equations, *Z. Angew. Math. Phys.* 33 (1982) 189–201.
- [14] Garg V.K., Rouleau W.T., Linear spatial stability of pipe Poiseuille flow, *J. Fluid Mech.* 54 (1972) 113–127.
- [15] Khorrani M.R., Malik M.R., Ash R.L., Application of spectral collocation techniques to the stability of swirling flows, *J. Comput. Phys.* 81 (1989) 206–229.
- [16] Tumin A., Receptivity of pipe Poiseuille flow, *J. Fluid Mech.* 315 (1996) 119–137.